






Project Hephaistos – II. Dyson sphere candidates from *Gaia* DR3, 2MASS, and *WISE*

Matías Suazo ^{1,★}, Erik Zackrisson ^{1,2,★}, Priyatam K. Mahto,³ Fabian Lundell,¹ Carl Nettelblad ⁴,
Andreas J. Korn,¹ Jason T. Wright ^{5,6,7} and Suman Majumdar ^{3,8}

¹Observational Astrophysics, Department of Physics and Astronomy, Uppsala University, Box 516, SE-751 20 Uppsala, Sweden

²Swedish Collegium for Advanced Study, Linneanum, Thunbergsvägen, 2 SE-752 38 Uppsala, Sweden

³Department of Astronomy, Astrophysics and Space Engineering, Indian Institute of Technology, Indore 453552, India

⁴Division of Scientific Computing, Department of Information Technology, Uppsala University, SE-751 05 Uppsala, Sweden

⁵Department of Astronomy & Astrophysics, The Pennsylvania State University, University Park, PA 16802, USA

⁶Penn State Extraterrestrial Intelligence Center, The Pennsylvania State University, University Park, PA 16802, USA

⁷Center for Exoplanets and Habitable Worlds, The Pennsylvania State University, University Park, PA 16802, USA

⁸Department of Physics, Blackett Laboratory, Imperial College, London SW7 2AZ, UK

Accepted 2024 April 30. Received 2024 April 29; in original form 2023 September 13

ABSTRACT

The search for extraterrestrial intelligence is currently being pursued using multiple techniques and in different wavelength bands. Dyson spheres, megastructures that could be constructed by advanced civilizations to harness the radiation energy of their host stars, represent a potential technosignature, that in principle may be hiding in public data already collected as part of large astronomical surveys. In this study, we present a comprehensive search for partial Dyson spheres by analysing optical and infrared observations from *Gaia*, 2MASS, and *WISE*. We develop a pipeline that employs multiple filters to identify potential candidates and reject interlopers in a sample of five million objects, which incorporates a convolutional neural network to help identify confusion in *WISE* data. Finally, the pipeline identifies seven candidates deserving of further analysis. All of these objects are M-dwarfs, for which astrophysical phenomena cannot easily account for the observed infrared excess emission.

Key words: extraterrestrial intelligence – infrared: stars.

1 INTRODUCTION

In the early 60s, Dyson (1960) proposed an innovative methodology for searching for signs of extraterrestrial life. He presumed that highly advanced civilizations, in the pursuit of more energy resources, would construct an artificial, light-absorbing structure around their host star. This hypothetical structure, later referred to as a ‘Dyson sphere’ (DS), would allow them to harvest energy in the form of starlight. Starlight harvesting could, in principle, result in different observational signatures that may be detected using existing telescopes. These signatures include optical dimming of the host star due to direct obscuration, and waste-heat emission from the absorbing structure (e.g. Dyson 1960; Wright et al. 2016; Wright 2020). Consequently, searching for anomalous infrared beacons in the sky has become an alternative to traditional communication-based searches for technologically advanced civilizations. One of the advantages of searches based on ‘Dysonian’ signatures is that it does not rely on the willingness of other civilizations to contact us.

Several observational projects have previously been conducted to detect individual DSs (e.g. Slysh 1985; Jugaku & Nishimura 1991; Timofeev, Kardashev & Promyslov 2000; Jugaku & Nishimura 2004;

Carrigan 2009; Zackrisson et al. 2018) and for the large-scale use of similar technology at extragalactic distances (Annis 1999; Wright et al. 2014a, b; Garrett 2015; Griffith et al. 2015; Zackrisson et al. 2015; Lacki 2016; Olson 2017; Chen & Garrett 2021). However, none of these searches have revealed any strong candidates for Dysonian technology.

Most search efforts have aimed for individual complete DSs, employing far-infrared (FIR) photometry (e.g. Slysh 1985; Jugaku & Nishimura 1991; Timofeev et al. 2000; Carrigan 2009) from the Infrared Astronomical Satellite (IRAS; Neugebauer et al. 1984), while a few considered partial DSs (e.g. Jugaku & Nishimura 2004). IRAS scanned the sky in the FIR, providing data of $\approx 2.5 \times 10^5$ point sources. However, nowadays, we rely on photometric surveys covering optical, near-infrared (NIR), and mid-infrared (MIR) wavelengths that reach object counts of up to $\sim 10^9$ targets and allow for larger search programs.

Within the context of *Project Hephaistos*,¹ in Suazo et al. (2022) we established upper limits on the prevalence of partial DSs in the Milky Way by analysing the fraction of sources from *Gaia* DR2 and the Wide-field Infrared Survey Explorer (*WISE*) that exhibit infrared excess. In total, more than 10^8 stars were analysed in that work. The exact upper limits on the fraction of stars that may host DSs reported

* E-mail: matias.suazo@physics.uu.se (MS); erik.zackrisson@physics.uu.se (EZ)

¹<https://www.astro.uu.se/~ez/hephaistos/hephaistos.html>

by Suazo et al. (2022) are a function of distance, covering fraction and DS temperature, but reach as low as ~ 1 in 100 000 objects in the most constraining situation. However, the actual fraction is likely to be much lower (and possibly 0 per cent) since a number of other effects, such as dust emission and source blending, may also give rise to anomalous infrared fluxes. Note that the Suazo et al. (2022) upper limits are derived from colour cuts rather than from fitting DS models to the data, since the aim of that paper was not to discuss the nature of individual sources of excess infrared radiation.

This second paper examines the *Gaia* DR3, 2MASS, and *WISE* photometry of ~ 5 million sources to build a catalogue of potential DSs. Here, we focus on the search for partial DSs, which partly obscure the starlight, which would still be detectable depending on the level of completion of the DS. This structure would emit waste heat in the form of MIR radiation that, in addition to the level of completion of the structure, would depend on its effective temperature. *Gaia* DR3 provides, unlike DR2, various astrophysical parameters derived from the low-resolution BP/RP spectra that can facilitate the rejection of false positives in the search for DSs.

Gaia, 2MASS, and *WISE* all provide photometric data in the optical, NIR, and MIR, respectively, but *Gaia* also provides parallax-based distances, which allow the spectral energy distributions (SEDs) of the targets to be converted to an absolute luminosity scale. The parallax data also make it possible to reject other point-like sources of strong MIR radiation such as quasars, but do not rule out stars with a quasar in the background.

Since excess thermal emission at MIR wavelengths represents the primary signature of DSs, searches for such objects naturally intersect with searches focused on MIR excess sources in general. Excess emission in the infrared is a valuable tracer of the circumstellar dust that has been heated by the starlight and is reemitted at longer wavelengths. Circumstellar dust is present in structures such as young stars (e.g. Kennedy et al. 2012; Kennedy & Wyatt 2013; Patel, Metchev & Heinze 2014; Cotten & Song 2016). Many searches seeking infrared excess sources have encountered various difficulties when using *WISE*/*AllWISE* data, including flux overestimation for sources near the saturation limit (Cutri et al. 2014), and the potential contamination from companion stars or background galaxies due to the large full width at half-maximum (FWHM) of the 12 and 22 μm point spread functions (PSFs; 6.5 and 12 arcsec, respectively; e.g. Kennedy et al. 2012; Theissen & West 2017).

It has been proposed that DSs and similar radiation-harvesting megastructures could be constructed around a variety of stellar-mass objects, including white dwarfs (Semiz & Oğur 2015; Zuckerman 2022), pulsars (Osmanov 2016, 2018), and black holes (Hsiao et al. 2021). Here, we limit the discussion to DSs around main-sequence stars. We additionally assume that feedback from DSs on to the host star may be neglected since this becomes relevant only when dealing with small, nearly completed DSs or with highly internally reflective structures. (Huston & Wright 2022).

In Section 2, we describe our overall search method. In Section 3, we present the most promising sources that emerged from our analysis, along with an examination of false positives encountered during the search. In Section 4, we discuss the likely nature of some of these DS candidates and how future follow-up observations can help us disentangle their true nature. Section 5 summarizes our results.

2 METHODS

This paper utilizes data from *Gaia* Data Release 3 (Gaia Collaboration 2016, 2023), 2MASS (Skrutskie et al. 2006), and *AllWISE* (Cutri et al. 2014). *Gaia* DR3 provides parallaxes and fluxes in three optical

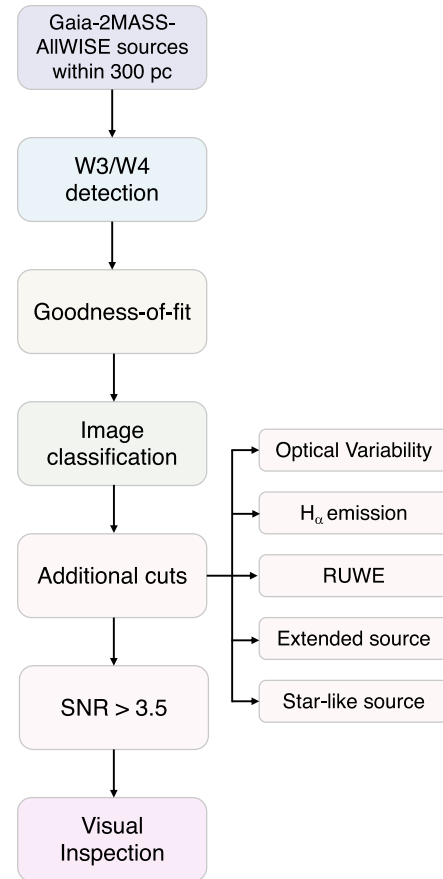


Figure 1. Flowchart illustrating our pipeline to find DS candidates.

bands (G_{BP} , G , G_{RP}) in addition to various astrophysical parameters derived from the low-resolution BP/RP spectra. 2MASS provides NIR fluxes in the J , H , and K_s bands, which corresponds to 1.2, 1.6, and 2.1 μm , respectively, while *WISE* provides MIR fluxes at the $W1$, $W2$, $W3$, and $W4$ bands which corresponds to 3.4, 4.6, 12, and 22 μm . The *AllWISE* program is an extension of the *WISE* program (Wright et al. 2010) and combines data from different phases of the mission.

A specialized pipeline has been developed to identify potential DS candidates, focusing on detecting sources that display anomalous infrared excesses that cannot be attributed to any known natural source of such radiation. It is essentially impossible to prove the existence of a DSs based on photometric data only, so this search can be considered a standard search for infrared excess sources biased towards excesses that are consistent with DSs based on their bright MIR fluxes and our models of what the SED of DSs should look like. A simple schematic representation of this pipeline is illustrated in Fig. 1.

The pipeline for identifying DS candidates involves several stages. We briefly describe each step:

(i) Data collection: We collect data from *Gaia*, 2MASS, and *AllWISE* for sources within 300 pc and detections in the 12 and 22 μm bands ($W3$ and $W4$ *WISE* bands).

(ii) Grid search: A grid search method is employed to determine each star's best-fitting DS model, utilizing the combined *Gaia*-2MASS-*AllWISE* photometry.

(iii) Image classification: To differentiate potential candidates located in nebular regions, a convolutional neural network (CNN)-

based algorithm is applied to *WISE* images to determine if our sources exhibit features associated with nebular regions. Young dust-obscured stars or stars otherwise associated with dusty nebulae appear as common false positives in our search. Therefore, only images lacking nebular features proceed to the next step.

(iv) Additional analysis: This step involves utilizing several *Gaia-WISE* flags to assess whether the stars might exhibit an infrared excess of natural origin.

(v) Signal-to-noise ratio (SNR): Many sources with low signal-to-noise ratios (SNR in *W3* and *W4*) slip through all the previous steps. Therefore, we manually include this step where all sources with SNR lower than 3.5 in the *W3* and *W4* bands are rejected.

(vi) Visual inspection: We visually inspect optical, NIR, and MIR images of all sources in order to reject problematic sources of MIR radiation. Blends are the most typical confounder in this step.

These steps filter out sources that do not exhibit the desired characteristics of a DS. Each step is explained in more detail in the following sections.

2.1 Data collection

We begin our search by taking a sample of stars from the *Gaia* DR3-2MASS-AllWISE catalogue. The cross-matching between these catalogues was done by simultaneously using the *allwise_best_neighbour*, *tmass_psc_xsc_best_neighbour*, and *tmass_psc_xsc_join* catalogs provided by the *Gaia* consortium. Within this sample, our focus was on selecting stars located within a distance of 300 parsecs (pc) based on the geometric distance derived in the Early Data Release 3 (EDR3; Bailer-Jones et al. 2021). We opted to utilize EDR3 distances rather than *Gaia* DR3 distances, as the latter is derived from low-resolution BP/RP spectra and is therefore not available for most stars in the sample.

Following the above mentioned criteria, our initial sample comprised approximately 5 million sources. Subsequently, we implemented an additional selection criterion, demanding detections in the 12 and 22 μm bands (*W3* and *W4*, respectively) from *WISE*. This choice was motivated by the fact that the expected infrared excess of DSs is particularly pronounced in these bands, given the range of temperature expected for DSs, as elaborated in Section 2.2. We additionally excluded sources that exhibited contamination according to the *WISE* contamination flag. As a result of this filtering step, our sample was downsized to approximately 320 000 stars.

2.2 Theory and models

The next step in our pipeline corresponds to determining how well the photometry of the stars in the catalogue resembles that of hypothetical main-sequence stars hosting DSs. This assessment requires understanding how the photometry of stars changes when surrounded by a DS, which involves two effects: the obscuration of the star by the DS and the re-emission of absorbed radiation by the structure at longer wavelengths. To predict the observational characteristics of a composite system consisting of a star and a DS (DS), we employ the model presented in Suazo et al. (2022). This model incorporates the expected photometric fluxes of a DS into the photometry of observed main-sequence stars to simulate the combined system. In simple terms, the photometry of a star is modified according to the following equation:

$$M = -2.5 \log(10^{-M_{\star}/2.5} + 10^{-M_{\text{DS}}/2.5}), \quad (1)$$

where M_{DS} represents the magnitude of the DS, and M_{\star} corresponds to the magnitude of the star after it has been obscured by the DS. It is important to note that this formula applies to both apparent and absolute scales and can be used in various magnitude systems.

To determine M_{DS} , we model the spectrum of the DS as a blackbody. Additionally, we assume that DSs behave as grey absorbers. Under these assumptions, the model star + DS depends on two free parameters: the covering factor (γ) and the effective temperature of the DS (T_{DS}). The covering factor γ is defined as the normalized luminosity of the DS:

$$\gamma = \frac{L_{\text{DS}}}{L_{\star}}, \quad (2)$$

where L_{DS} is the luminosity of the DS and L_{\star} is the luminosity of the star hosting the DS before being obscured. Under this definition, γ can only be a positive number lower or equal to 1. In the case of an isotropically radiating star, γ also represents the fractional solid angle of outgoing radiation intercepted by the DS (the covering factor) or the DS's completion level if we assume that the structure is nearly spherical. With all this information, we can determine the magnitude of the star when it is obscured by the DS using the following equation:

$$M_{\star} = M_{\star,0} - 2.5 \log_{10}(1 - \gamma), \quad (3)$$

where $M_{\star,0}$ is the magnitude of the star before being obscured. In practice, we take $M_{\star,0}$ values from main-sequence stars in the *Gaia*-2MASS-AllWISE photometry as described below.

In summary, equations (1) and (3) provide a framework for understanding the changes in the magnitude of a star if it were hosting a DS. These equations describe the transformation from the original magnitude $M_{\star,0}$ to the modified magnitude M when considering a DS with a given temperature T_{DS} and covering factor γ . We also assume that DSs are built up slowly and uniformly everywhere, with equal covering factor (γ) in every direction, with no pieces large enough to cause stellar variability, see Section 2.5.2. An interesting feature of this model is that it is identical to optically thin blackbody debris disc models, where the covering factor γ resembles the fractional luminosity ($L_{\text{Disk}}/L_{\star}$). Fig. 2 illustrates examples of the photometry of a Sun-like star ($T_{\text{eff}} = 5777$ K) hosting DSs with various parameters. In the top panel, the composite spectrum is shown for a fixed DS temperature of 300 K and covering factors of $\gamma = 0.1, 0.5,$ and 0.9 , while the bottom panel displays the spectrum variations for a fixed covering factor of 0.5 and DS temperatures of 100, 300, and 600 K. The main signatures produced by a DS include a drop in stellar flux and a boost of the flux in the MIR, where the MIR peak depends on the temperature of the DS. The figure demonstrates how the crucial infrared information required for the identification of DS candidates is contained within the *W3* and *W4* bands, as mentioned in Section 2.1. Consequently, we demand that all stars that undergo our analysis have detections in both *W3* and *W4* bands.

Although the temperature of the DS is a free parameter, we limit our search to DS temperatures ranging from 100 to 700 K to align with *WISE*'s infrared detection capabilities. Additionally, we consider covering factors equal to or greater than 0.1, as this threshold ensures significant infrared excess for detection, as shown by Suazo et al. (2022). In total, we generated 220 745 DS models by simulating how the *Gaia*-2MASS-*WISE* photometry of 265 main-sequence stars would change in the presence of DSs according to the presented models. We select main-sequence stars with M_G values ranging from 0 to 13.6 (stellar effective temperatures from ~ 2800 to 12 500 K) and ensure that these are main-sequence stars as explained in Appendix A. We also ensure that these stars already do not possess any MIR excess.

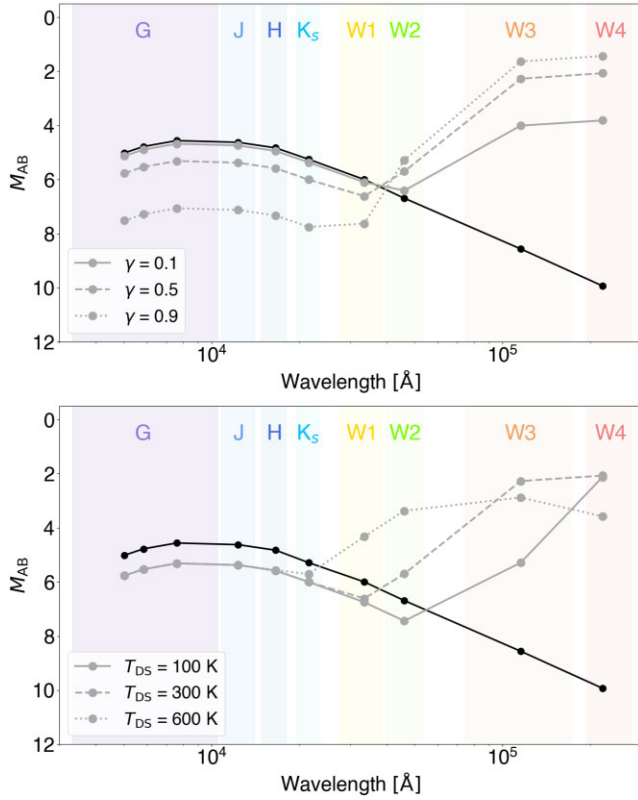


Figure 2. Modified photometry of a Sun-like star in the *Gaia*-*WISE*-*2MASS* bands due to the presence of various DSs. The unmodified absolute magnitudes of the Sun-like star ($T_{\text{eff}} = 5777$ K) are represented by solid black lines. In the top panel, the DS models have an effective temperature of $T_{\text{DS}} = 300$ K and covering factors of 0.1, 0.5, and 0.9, depicted by solid grey, dashed, and dotted lines, respectively. In the bottom panel, the DS models have a fixed covering factor of $\gamma = 0.5$ and temperatures of 100, 300, and 600 K, depicted by solid grey, dashed, and dotted lines, respectively. The coloured bands in the plots represent the wavelength ranges detectable by the *Gaia*, *2MASS*, and *WISE* missions. It is important to note that the absolute magnitudes depicted in these plots are in the AB system.

2.3 Grid search

After generating the 220 745 models, we proceeded to compare the photometry of all remaining main-sequence stars from Section 2.1 to these models. This involves performing a grid search to find the best-fitting model for each of the 320 000 sources. The selection of the best-fitting model for each star was based on minimizing the root mean squared error (RMSE) between the observed data and the model predictions.

Following the search for the best models, we filtered out all stars whose best model yielded an RMSE higher than 0.2 mag. This selection is quite simple and does not consider the error measured since, otherwise, it would prioritize better fits in the optical rather than in the MIR, where the information of the infrared excess lies in this work. The selection of this threshold is a free parameter. Still, we chose it to be 0.2 mag to reduce the sample of potential candidates to a reasonable number that we could potentially aim to follow up with additional observations on a reasonable time-scale. Additionally, the selection of this threshold is motivated by comparing our models with Vioque et al. (2020) pre-main sequence, classical Be stars, and sources that have been proposed as candidates of these two categories based on different features (photometry, optical variability, etc.), but have not yet been confirmed. We assessed what RMSE threshold

Table 1. Convolutional neural network architecture.

Layer	Layer parameters	Output size
Input		$420 \times 420 \times 1$
Convolution ^{a, b}	$3 \times 3, 6$	$418 \times 418 \times 6$
Max pooling	$2 \times 2, \text{Stride } 2$	$209 \times 209 \times 6$
Convolution ^{a, b}	$3 \times 3, 12$	$207 \times 207 \times 12$
Max pooling	$2 \times 2, \text{Stride } 2$	$103 \times 103 \times 12$
Convolution ^{a, b}	$3 \times 3, 32$	$101 \times 101 \times 32$
Max pooling	$2 \times 2, \text{Stride } 2$	$50 \times 50 \times 32$
Convolution ^{a, b}	$3 \times 3, 64$	$48 \times 48 \times 64$
Max pooling	$2 \times 2, \text{Stride } 2$	$24 \times 24 \times 64$
Convolution ^{a, b}	$3 \times 3, 128$	$22 \times 22 \times 128$
Flatten		61 952
Fully connected network		
First hidden layer ^{a, b, c}	$61\,952 \times 256$	256
Second hidden layer ^{a, b, c}	256×256	256
Third hidden layer ^{a, b, c}	256×256	256
Softmax	256×2	2

Note. ^aBatch normalization is applied. ^bThe ReLU activation function is applied. ^cA dropout regularization was applied.

value is reasonable by comparing our models to the photometry of the stars presented in this catalogue. Since pre-main sequence stars and classical Be stars are known to be significant sources of MIR emission and therefore represent potential interlopers in our search. Most stars in the Vioque et al. (2020) catalogue that we examined displayed an RMSE higher than 0.2 mag when compared to our models, so we used this threshold as our goodness-of-fit criterion to select potential candidates. We found $\sim 11\,000$ sources whose best fit suffices an RMSE lower than 0.2.

After filtering the stars based on the RMSE criterion, we proceeded to classify the remaining sources using a neural network. This classification aimed to distinguish whether the sources were located in nebular regions. Nebulae can generate features that are similar to those hypothetically produced by a DS, hence the motivation behind developing this algorithm.

2.4 Image classification

Upon selecting candidates using an RMSE as our goodness-of-fit metric, we found that young dust-obscured stars or stars otherwise associated with prominent nebulae appear as common false positives. Previous searches for infrared sources (e.g. Kennedy et al. 2012; Ribas et al. 2012) encountered contamination issues due to the presence of foreground or nearby sources, which can cause large photocentre shifts across all *WISE* bands and/or an extended morphology. All these phenomena can produce photometric signatures that resemble those of our models. To reduce the number of interlopers in the form of young obscured stars in our sample, we developed an algorithm to classify whether stars lie or not in nebular areas based on their *WISE* images. This algorithm utilizes normalized *W3* images as input and aims to classify stars based on whether they reside in nebular regions. The CNN architecture employed in this work is presented in Table 1, and it was developed using the *PYTORCH* library (Paszke et al. 2019).

Our algorithm's input images were standardized to 420×420 pixels, with each pixel representing a square of side 1.375 arcsec. This corresponds to a squared image with a side of 9.625 arcmin. Then, we classified 960 images by ocular inspection, with half of them depicting images of stars embedded in nebulae and the other half representing non-nebular cases. In Fig. 3, we provide examples

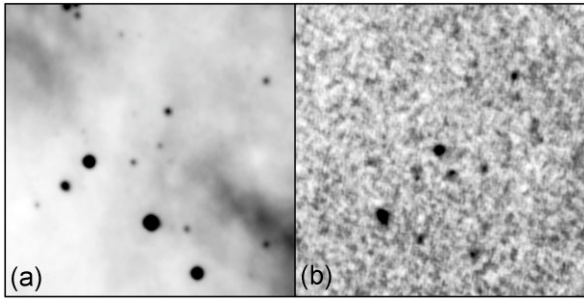


Figure 3. Two images exemplify each category’s appearance: Nebular on the left-hand side panel and non-nebular on the right-hand side. Both images are normalized. Each image corresponds to a squared region in the sky with a side of 9.625 arcmin.

Table 2. Hyperparameter random search values.

Hyperparameter	Random search values
Learning rate	10^{-3} , $5 \cdot 10^{-4}$, 10^{-4} , $5 \cdot 10^{-5}$
Regularization parameters (β_1 , β_2)	0, 0.3, 0.5, 0.7, 0.9, 0.99
Dropout probability p	0, 0.2, 0.4, 0.6
Number of neurons	32, 128, 256
Kernel size	3, 5, 7

of two images that were classified as nebular and non-nebular. We split our sample into the training, validation, and testing subsets. All subsets were built by selecting random images in our sample. Training, validation, and testing sets were randomly sampled and split into 70 per cent, 15 per cent, and 15 per cent of the total data set, respectively.

We do not include $W1$ nor $W2$ bands since dusty nebular features are typically not detectable in these bands. We also omit the $W4$ images since these tend to have lower quality and do not provide much extra information compared to $W3$.

The specific CNN architecture used in this work is presented in Table 1. For the convolutional layers, the parameters shown in Table 1 are the filter dimensions and the number of output channels. No padding was applied to any of the convolutional layers. Moreover, to all the convolutional and fully connected layers, a rectified linear unit (ReLU; Nair & Hinton 2010) activation function was applied, except for the last fully connected layer, which utilized a softmax function instead. Additionally, we ‘batch normalized’ (Ioffe & Szegedy 2015) every layer after convolution. The output of the last convolutional layer is flattened to feed the fully connected layers. We additionally applied a dropout regularization after each layer in the fully connected network (Hinton et al. 2012). We seek the minimum of the loss function by using the Adam algorithm (Kingma & Ba 2014). The network was trained using batches of 64 images.

To optimize the performance of our classifier, we conducted a hyperparameter search by randomly sampling 79 out of the 5184 possible combinations of the parameters listed in Table 2. The parameters that were tuned include the learning rate, the beta parameters (β_1 and β_2) of the Adam algorithm, the dropout probability (p), the number of neurons in the fully connected network, and the kernel size in the convolutional matrices.

The learning rate controls the magnitude of weight updates during training, whereas the beta parameters β_1 and β_2 are decay rates used to estimate the moments of the gradient for finding the global minimum of the loss function. The dropout probability p determines

the probability of zeroing out a neuron in a layer to prevent overfitting. The number of neurons in the fully connected network determines the number of units in each hidden layer. It is important to note that the learning rate and beta parameters are related to the training process, while the dropout probability and the number of neurons per hidden layer are design parameters of the architecture.

We trained nine networks for each combination of hyperparameters with different initial random weights. The initial weights are sampled from the uniform distribution that PYTORCH has implemented to initialize weights. Additionally, each network was trained during 35 epochs. After evaluating 79 random hyperparameter combinations, we found several combinations that yielded accuracies ~ 93 per cent on the validation set. A family of neural networks with similar characteristics and performances was identified, and the specific hyperparameters of this family and their performance are shown in Table 3. Accuracies are reported on the testing set.

From the family of neural networks with similar performances, we selected the architecture that achieved the highest mean accuracy and the lowest standard deviation. In this case, it corresponds to experiment F in Table 3. Additionally, in Fig. 4, we show the confusion matrix for the testing set in the best run for this architecture. The accuracy is 0.95, the recall is 0.975 on the non-nebular class, and the precision is 0.93 on the non-nebular class.

Using the trained CNN, we proceeded to classify whether stars lie or not in the nebular region. We find that 5732 sources appear as sources in non-nebular regions according to our classifier.

2.5 Additional analysis

In the next subsections, we introduce additional criteria and cuts to refine further and validate our selection of DS candidates among the sources exhibiting an infrared excess. These criteria help us rule out false positives and ensure we focus on the most promising candidates.

2.5.1 $H\alpha$ emission

The emission of $H\alpha$ photons is an important signature of young stars, particularly during strong accreting episodes. When a young protostar heats up, it ionizes the surrounding hydrogen-dominated accretion disc, which ends up emitting $H\alpha$ photons (Barrado y Navascués & Martín 2003).

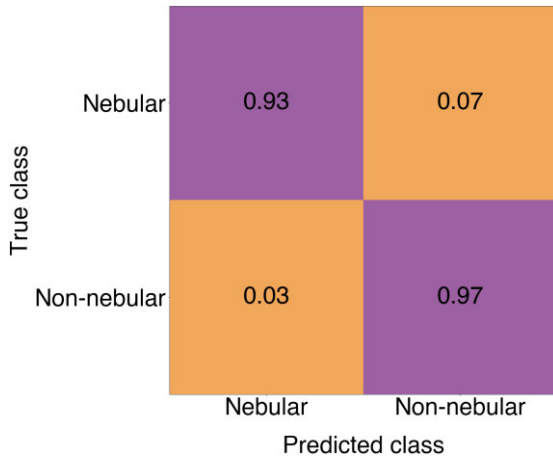
In *Gaia* DR3, the pseudo-equivalent width (EW) of $H\alpha$ is provided as one of the new products (Creevey et al. 2023; Fouesneau et al. 2023), and it becomes one of the most important parameters when weeding out interlopers. Just as optical variability is a characteristic feature of pre-main-sequence stars, the emission of $H\alpha$ photons due to hydrogen excitation during the accretion process is another significant signature. To filter out false positives, sources with $H\alpha$ EWs lower than zero (at 3σ) are rejected, i.e. sources with $H\alpha$ emission detected at 99.7 per cent confidence.

2.5.2 Optical variability

Pre-main-sequence stars, being in the early stages of stellar evolution, can naturally emit infrared radiation due to the presence of an accretion disc surrounding the forming star. These young stars often exhibit brightness variability as a characteristic feature (e.g. Joy 1945; Herbst et al. 2007). The variability can be attributed to various factors, including circumstellar obscuration events, hotspots on the star or disc, accretion bursts, and rapid structural changes in the accretion disc (Cody et al. 2014).

Table 3. Best hyperparameter combination.

Label experiment	Learning rate	β_1	β_2	Dropout probability	Number of neurons	Kernel size	Average accuracy	Standard deviation accuracy
A	5×10^{-4}	0.5	0.9	0.6	256	3	0.916	0.031
B	10^{-4}	0.5	0.5	0.6	128	3	0.913	0.017
C	10^{-4}	0.5	0.9	0.6	128	3	0.915	0.029
D	5×10^{-4}	0.5	0.9	0.6	128	3	0.908	0.020
E	10^{-4}	0.5	0.5	0.6	256	3	0.906	0.034
F	5×10^{-4}	0.5	0.5	0.6	256	3	0.930	0.016

**Figure 4.** Normalized confusion matrix for the test set using the architecture yielding the best results. The test set contains 144 elements.

Gaia DR3 provides an optical variability flag among other newly added products. However, this flag is unavailable for most sources. In order to assess the optical variability of stars, we ourselves constructed the observable G_{var} , which is defined in Vioque et al. (2020). This observable aims to quantify the level of optical variability and has been used to classify different types of variable stars, including Herbig Ae/Be stars, TTauri stars, and classical Be stars. The observable G_{var} is defined as

$$G_{\text{var}} = \frac{F'_G e(F_G) \sqrt{N_{\text{obs},G}}}{F_G e'(F_G) \sqrt{N'_{\text{obs},G}}}, \quad (4)$$

where F_G and $e(F_G)$ are the *Gaia* G -band flux and its uncertainty, respectively, while $N_{\text{obs},G}$ corresponds to the number of times that source was observed in the G band. The logic behind this formula relies on the fact that variable sources should have larger uncertainties compared to non-variable ones. The denominator refers to the median value of sources with similar fluxes since non-variable objects exhibit different uncertainties. Vioque et al. (2020) showed that pre-main-sequence stars exhibit a wide range of G_{var} that goes from ~ 0.7 to ~ 100 . The distribution of G_{var} for known pre-main-sequence stars peaks at $G_{\text{var}} \sim 6$, and it decreases towards the above-mentioned values. Here, we reject all stars exhibiting a G_{var} higher than two, since they are most likely to be young stars. Similarly, Barber & Mann (2023) developed a proxy for stellar variability and age, indicating that *Gaia* excess photometric uncertainties decrease linearly with $\log_{10}(\text{age})$ in Myr. However, this relation primarily applies to FGK and early M-type stars. These studies demonstrate the potential of using *Gaia* uncertainties and variability measures to infer the ages and variability status of stars.

It is important to note that this check rejects potential Dyson swarms with very large absorbing elements since these in principle could generate detectable variations in the photometry of the host star. However, these variations could be mistaken for other astrophysical phenomena such as asteroseismic variations or photometric noise (Wright et al. 2016). It is also practical to exclude variable sources; otherwise, young stars would more easily slip through our pipeline.

2.5.3 Astrometry

Our search strongly relies on parallax-based distances, which can be incorrectly estimated if the single-star model fails to fit the astrometric observations. In order to assess the reliability of the distance, *Gaia* provides the Renormalised Unit Weight Error (RUWE), a parameter that tells us how well astrometric observations fit the astrometric solution. RUWE values tend to be close to 1.0 for well-behaved sources, while significantly higher values exceeding 1.0 may indicate non-single or problematic sources. To ensure reliable astrometry, we implemented a conservative RUWE threshold of 1.4. Sources surpassing this threshold are excluded as potential candidates to minimize objects with unreliable distance estimates. Other studies (e.g. Stassun & Torres 2021) have shown a significant correlation between the RUWE statistic and unresolved binary systems. Binary systems can generate warm dust through processes such as the catastrophic collision of planets (e.g. Weinberger 2008; Thompson et al. 2019). Given that such systems might have inaccurate distances and exhibit MIR flux excess, the aforementioned RUWE criterion aids in rejecting sources potentially comprising binaries surrounded by warm dust, as well as those with problematic astrometry.

2.5.4 Extended sources

We expect all candidates to have a shape consistent with a point source therefore we rule out all sources having a non-zero AllWISE *ext_flag*.

2.5.5 Star probability

Gaia also classifies sources into different categories. We use one of the probability metrics *Gaia* DR3 provides to ensure the source is more likely to be a star. In particular, we use *classprob_dsc_combmod_star* > 0.9 to consider our source candidates. We found no difference when comparing similar classification metrics.

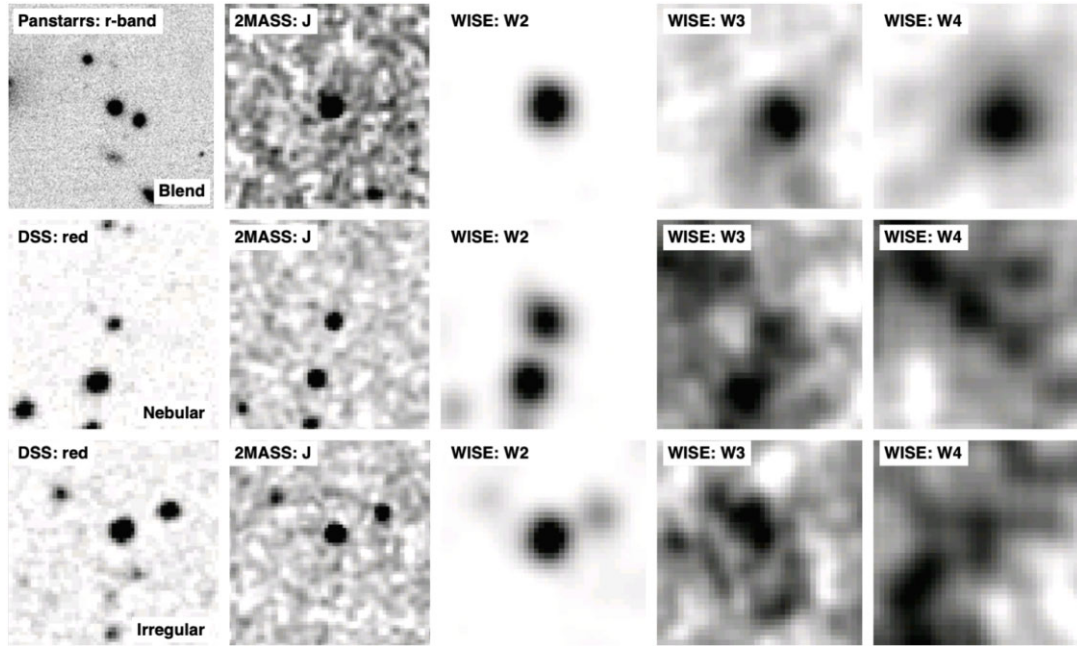


Figure 5. Examples of typical confounders in our search. The top row features a source from the blends category, the middle row a source embedded in a nebular region, and the bottom row a case from the irregular category. On these scales, the irregular and nebular cases cannot be distinguished, but the nebular nature can be established by inspecting the images at larger scales.

2.5.6 Sources rejected so far

Out of all the criteria outlined in Section 2.5, the RUWE criterion refutes the largest quantity of candidates. A total of 282 sources are rejected by this criterion alone, which corresponds to roughly half of all sources rejected by any criteria in Section 2.5. The $H\alpha$ emission, the optical variability, and the extended flag criteria equally contribute to the rest of the cuts. We noticed that over 1000 sources have negative $H\alpha$ EWs. However, the uncertainties are so large that we cannot confirm $H\alpha$ emission at the 3σ level.

2.6 SNR criterion

After applying all the cuts presented in Section 2, we ended up with 5137 sources with DS-like SEDs. Consequently, we proceeded to visually inspect some of the $W3/W4$ images of these candidates. This step revealed that most of them appeared to be unconvincing as secure point-like sources. In many cases, these sources appear irregular or blend with the background noise. Although *WISE* data reduction considers any signal with an SNR value higher than 2 as a detection, many of these detections are not reliable and fail to represent genuine infrared sources; most of the inspected images matched this pattern. Therefore, an additional cut was applied based on the SNR of these ~ 5000 sources. We selected sources with SNR higher than 3.5 in both the $W3$ and $W4$ bands, resulting in 368 sources.

2.7 Visual inspection

After rejecting all sources with low SNRs, we conducted a second pass of visual inspections for all sources that survived the SNR cut. Visual examination of *WISE* images (e.g. Ribas et al. 2012; Sgro & Song 2021) is a common technique to identify and reject unreliable sources, as not all flags or metrics provided by *WISE* can address issues in the data reduction. Following scrutiny of all *WISE* images, we categorized three types of confounders: blends, irregular

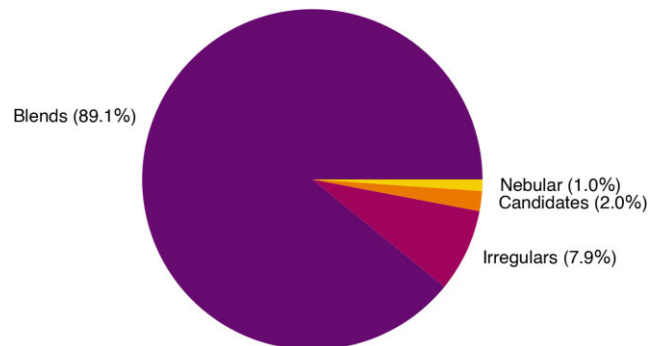


Figure 6. Pie chart illustrating the cause of infrared radiation according to our extra inspection.

structures, and nebular features. Fig. 5 illustrates the distinctions between these classes. In the top row, we showcase the ‘blend case,’ where a source overlaps with external sources within the aperture of the *WISE* bands, particularly noticeable in the $W3$ and $W4$ bands. Optical images with higher resolution facilitate the detection of blends. Even if some contaminants do not emit optical light, if an infrared source appears significantly shifted from the image centre and lacks optical emission, it is considered a blend and subsequently rejected.

In the second row of Fig. 5, we depict the ‘nebular’ category of false positives. These cases exhibit $W3$ and $W4$ images that appear hazy and disordered, lacking a discernible source of infrared radiation at the location of the candidate. However, upon examining large-scale images spanning approximately 600 arcsec, distinctive nebular features become evident. Some of these features resemble the example shown in Fig. 3. These confounding sources are instances where our CNN (Section 2.4) failed to reject these sources accurately. In the third row, we illustrate the ‘Irregular’ category,

Table 4. Number of stars after every cut.

Stage	Number of stars
Stars in Gaia DR3-2MASS-AllWISE within 300 pc	$\sim 5 \times 10^6$
W3/W4 detection	$\sim 3.2 \times 10^5$
RMSE ≤ 0.2	11 243
Nebular classifier	5732
Extra cuts	5137
SNR W3/W4 > 3.5	368
Final candidates	7

which encompasses all sources that deviate from a point-like source in their W3 and W4 bands despite being selected based on having *WISE* *ext_flag* values equal to 0. In this category, the sources of irregularities in our candidates' W3 and W4 images are unclear, and there seems to be no indication of nebulosity in their surroundings when looking at larger-scale images. Causes of irregularities could be attributed to faint nebular features, high noise, and blends, but it is challenging to pinpoint the exact cause of this phenomenon. Most sources rejected in the SNR criterion had *WISE* images that would have fallen into this category.

Among the 368 sources that survived the last cut, we identified 328 (89.1 per cent) sources as blends, 29 (7.9 per cent) as irregulars, and 4 as nebular (1.0 per cent). After this analysis, a total of 7 (2.0 per cent) sources were identified as potential candidates that appear to be free of conspicuous problems. The visual inspection results are summarized in Fig. 6. Many blends were identified thanks to the inspection of optical images, so we double-checked that our seven final sources were free of contaminants by examining Pan-STARRS1 DR1 (Chambers et al. 2016) and Sky Mapper DR2 (Onken et al. 2019) images to account for both hemispheres. None of these seven sources showed any indication of contamination. Table 4 summarizes how the initial sample downsized after every step.

Finally, for the seven sources identified as potential candidates, we conducted a search for nearby X-ray sources. X-rays are a powerful tool for tracing star-forming regions in the sky (e.g. Sciortino 2022), suggesting our candidates could be young stars if X-ray sources associated with star formation were present in their vicinity. After searching the *XMM-Newton* science archive, we found no evidence of X-ray sources in the neighborhood of our candidates that could be attributed to star formation. In one instance, there is an X-ray source approximately 14 arcmin from a candidate; however, this source is confirmed to be a Seyfert galaxy.

3 RESULTS

In Table 5, we summarize all candidates. Our visual inspection indicates that these sources are actual sources of infrared radiation that are not subject to any obvious contamination. Given the limited number of candidates, we revised our model fitting using a more refined grid compared to the one employed in Section 2.3. This time, we compared our data to 6216 900 models, encompassing 391 DS effective temperatures ranging from 10 to 400 K and 60 covering factors ranging from 10^{-4} to 0.4. Table 5 presents the updated DS temperature estimates and covering factors.

While examining the pseudo-EW of $H\alpha$, we observed that some candidates exhibit too high uncertainties. Hence, there remains a possibility that some of these sources are indeed $H\alpha$ emitters, which would reveal the early stellar evolutionary stage and explain their infrared radiation. Fig. 7 showcases the SEDs and photometric

images of two of the seven candidates, while Table 5 provides additional information used in our further analysis (Section 2.5). In the examples depicted in Fig. 7, clear W3/W4 images indicate a distinct source of MIR radiation in both bands. Candidate A notably displays a considerable shift between DSS, 2MASS, and the *WISE* images, which is attributed to its relatively high proper motion. According to *Gaia* DR3, this star has a proper motion of -88.7 mas yr $^{-1}$ in declination.

3.1 Potential contamination

In this search, we encountered various sources of false positives, as detailed in previous sections. As highlighted in earlier studies (e.g. Kennedy et al. 2012; Krivov et al. 2013; Gáspár & Rieke 2014), Galactic background contamination and chance alignments with extragalactic sources can induce a false infrared excess at the location of a star. In the context of investigating *WISE* infrared stars within the Kepler field of view, Kennedy et al. (2012) found that the Improved Processing of the IRAS Survey (IRIS: Miville-Deschênes & Lagache 2005) offers valuable insights into potential background contamination. They identified that sources within regions where the $100 \mu\text{m}$ background level exceeded 5 MJy/sr were susceptible to galactic contamination. To assess whether our DS candidates were prone to such contamination, we utilized the IRIS maps at $100 \mu\text{m}$ to evaluate the background level of our sources. Table 6 summarizes these values, all of which fall below the threshold suggested by Kennedy et al. (2012). This result stems from our procedure of filtering out all stars embedded in nebular regions, thereby naturally eliminating sources located in regions where the Galactic background level affects the *WISE* photometry of stars.

In addition to background contamination, chance alignments with bright sources in the infrared but obscured in the optical present another potential contamination source. Kennedy et al. (2012) estimated the likelihood of such alignments by comparing galaxy counts with the counts of their infrared excess sources. As our DS candidates are limited to only seven, we adopted a method akin to that used by Theissen & West (2017). In their study, which investigates the presence of warm dust around M dwarfs, Theissen & West (2017) reanalysed the source extraction of their targets to determine offsets among their W1, W2, and W3 images. These offsets were then compared to the inherent offset of stationary objects like quasars. Quasars serve as valuable indicators of the *WISE* instrument's astrometric precision as they remain stationary in the sky. Theissen & West (2017) focused solely on isolated quasars (with no other sources within 6 arcsec), with W3 SNRs between 3 and 5, at galactic latitudes higher than 77 deg. They noted that the offset distributions resembled those of their disc candidate stars, both exhibiting Gaussian distributions. One distribution reflected the Right Ascension offset between the W1 and W3 positions ($\mu = 0''.08$, $\sigma = 5''.00$) and another for the Declination offset between the W1 and W3 positions ($\mu = -0''.21$ a, $\sigma = 5''.48$).

In order to assess the probability of chance alignments with extragalactic sources, we adopted a similar approach and re-conducted the source extraction to determine the offset between W1, W2, and W3 images. Initially, we obtained unWISE images of our candidates. unWISE (Lang 2014) provides a collection of *WISE* co-added images that remain unblurred, preserving their intrinsic resolution. Subsequently, we performed a revised source extraction using the SEP software (Barbary 2016), a PYTHON implementation that encompasses the core algorithms of Source Extractor (SEXTRACTOR; Bertin & Arnouts 1996).

Table 5. DS candidates. All sources are clear MIR emitters with no clear contaminants or signatures that indicate an obvious MIR origin.

Label	<i>Gaia</i> DR3 ID	Distance ^a (pc)	m_G^b	G_{var}^c	RUWE ^b	T_{eff}^b (K)	EW $H\alpha^b$ (nm)	T_{DS}^c (K)	γ^c	S/N ^d (W3/W4)
A	3 496 509 309 189 181 184	142.9 ± 1.0	15.99	1.03	1.03	–	0.248 ± 0.076	138 ± 6	0.08 ± 0.01	22.5/16.6
B	4 843 191 593 270 342 656	211.6 ± 3.5	17.71	0.94	1.06	3574	–	275 ± 40	0.06 ± 0.008	13.9/3.8
C	4 649 396 037 451 459 712	219.4 ± 6.2	18.39	0.90	1.21	3238	–	187 ± 16	0.14 ± 0.016	10.5/5.0
D	2 660 349 163 149 053 824	211.5 ± 5.8	17.66	0.97	0.96	3473	–	178 ± 20	0.16 ± 0.03	10.4/4.8
E	3 190 232 820 489 766 656	274.7 ± 6.1	17.00	0.90	1.05	3556	0.049 ± 0.100	180 ± 26	0.08 ± 0.02	10.3/3.6
F	2 956 570 141 274 256 512	265.0 ± 2.6	16.32	0.93	1.01	3674	0.020 ± 0.068	137 ± 16	0.03 ± 0.008	5.7/4.5
G	2 644 370 304 260 053 376	249.9 ± 3.7	16.48	0.99	1.01	3480	0.024 ± 0.097	100 ± 9	0.13 ± 0.02	5.0/3.5

Note. We present data derived from: ^a*Gaia* EDR3 Bailer-Jones et al. (2021). ^b*Gaia* DR3. ^cThis work. ^dAllWISE Cutri et al. (2014).

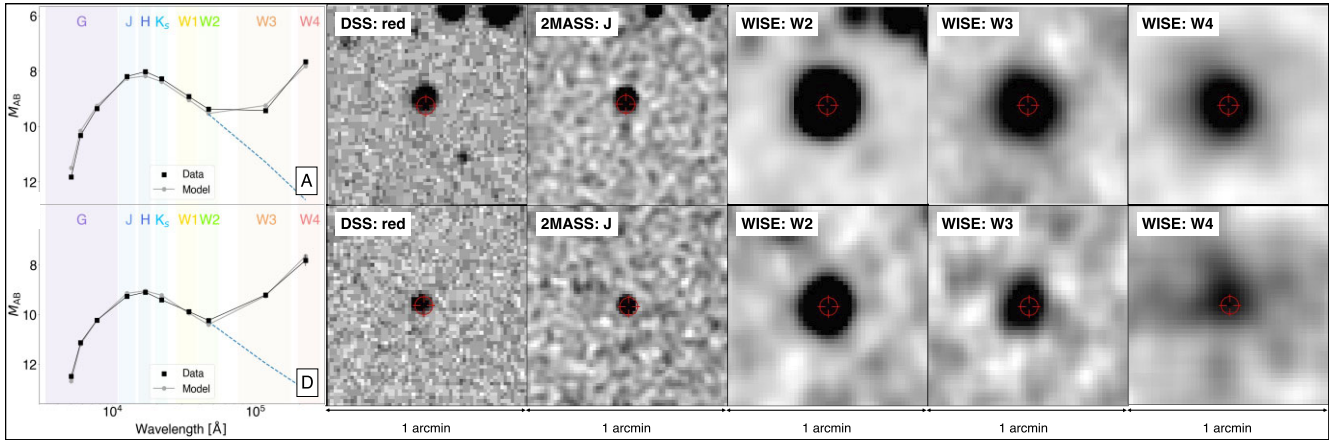


Figure 7. SEDs of our two DS candidates and their photometric images. The SED panels include the model and data, with the dashed lines indicating the model without considering the emission in the infrared from the DS and the solid black line indicating the model that includes the infrared flux from the DS. Photometric images encompass one arcmin. All images are centred in the position of the candidates, according to *Gaia* DR3. All sources are clear MIR emitters with no clear contaminants or signatures that indicate an obvious MIR origin. The middle circle marks the location of the star according to *Gaia* DR3.

Table 6. DS candidates and their 100 μm background level.

Label	<i>Gaia</i> DR3 ID	IRIS 100 μm background level (MJy/sr)
A	3 496 509 309 189 181 184	4.77
B	4 843 191 593 270 342 656	1.34
C	4 649 396 037 451 459 712	4.75
D	2 660 349 163 149 053 824	4.17
E	3 190 232 820 489 766 656	4.45
F	2 956 570 141 274 256 512	1.78
G	2 644 370 304 260 053 376	2.92

Table 7. Offset in the photocentre of our sources in different *WISE* bands.

Label	<i>Gaia</i> DR3 ID	W1/W2	W1/W3
		offset (arcsec) RA/DEC	offset (arcsec) RA/DEC
A	3 496 509 309 189 181 184	−0.25/−0.01	−0.03/0.33
B	4 843 191 593 270 342 656	0.40/0.31	3.21/0.06
C	4 649 396 037 451 459 712	0.25/−0.32	1.52/−3.68
D	2 660 349 163 149 053 824	−0.31/−0.12	0.60/−0.09
E	3 190 232 820 489 766 656	−0.09/0.48	−1.15/−0.38
F	2 956 570 141 274 256 512	0.03/0.10	−1.04/0.79
G	2 644 370 304 260 053 376	0.24/0.00	5.59/0.64

Table 7 summarizes the offsets between the positions of the extracted sources in different filters. It is noteworthy that for the W1–W2 offset, both in RA and DEC, the discrepancy is minimal and falls within the range obtained by Theissen & West (2017) in

both RA and DEC. Similarly, the offsets between the W1 and W3 bands also align with the distribution, except for candidate G, which appears suspicious and warrants careful consideration. However, the current data set lacks definitive evidence to either confirm or dismiss this candidate.

4 DISCUSSION

We conducted a comprehensive search for sources exhibiting SEDs compatible with stars hosting partial DSs. The last search of this kind was carried out by Carrigan (2009), who only looked for complete DSs ($\gamma = 1$) using IRAS data. We analysed a significantly larger sample of approximately 320 000 sources from the *Gaia* DR3–2MASS–AllWISE data set with W3/W4 detection, which is nearly 30 times larger than Carrigan’s sample. As a result, we identified seven sources displaying MIR flux excess of uncertain origin. Various processes involving circumstellar material surrounding a star, such as binary interactions, pre-main-sequence stars, and warm debris discs, can contribute to the observed MIR excess (e.g. Cotten & Song 2016). Kennedy & Wyatt (2013) estimate the occurrence rate of warm, bright dust. The occurrence rate is 1 over 100 for very young sources, whereas it becomes 1 over 10 000 for old systems (>1 Gyr). However, the results of our variability check suggest that our sources are not young stars. If our candidates were young stars, that could explain the infrared excess and would match the more likely occurrence rate. Nevertheless, it is worth noting that although uncommon, literature has documented the existence of pre-main-sequence stars with low G_{var} values (e.g. Vioque et al. 2020). On the other hand, our astrometric checks, which heavily rely

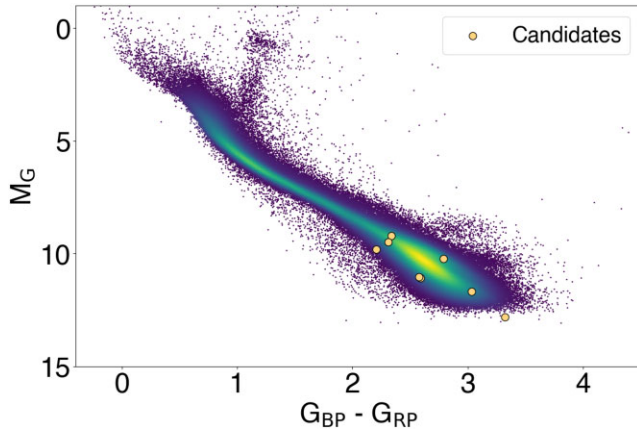


Figure 8. Colour–magnitude diagram displaying the distribution of our candidates in big circles. Small dots represent *Gaia* DR3 stars within 300 pc. The colour scale represents the relative density of stars.

on the RUWE parameter, indicate that the single-star astrometric solution is applicable to our sources. Despite the fact that we chose conservative thresholds for the G_{var} and RUWE parameters (2 and 1.4, respectively), our candidates have values that lie far below the thresholds chosen. The G_{var} and RUWE values are typically around unity.

The presence of warm debris discs surrounding our candidates remains a plausible explanation for the infrared excess of our sources. However, our candidates seem to be M-type main-sequence stars, given their stellar parameters and location in the Hertzsprung–Russell diagram as Fig. 8 illustrates. However, M-dwarf debris discs are very rare objects, and up to date, only a reduced number has been confirmed (e.g. Luppe et al. 2020; Cronin-Coltsmann et al. 2022, 2023). Multiple explanations have been invoked to explain the dearth of debris discs around M dwarfs, including detection biases (Heng & Malik 2013; Kennedy et al. 2018) and age biases (Riaz, Mullan & Gizis 2006; Avenhaus, Schmid & Meyer 2012). Additionally, studies have suggested that the physical processes governing debris disc evolution around M dwarfs may differ significantly from those observed in solar-type stars (Plavchan, Jura & Lipsy 2005). However, the temperature and the fractional infrared luminosity ($f = L_{\text{IR}}/L_{\star}$) of our candidates are different from those of typical debris discs, which tend to be cold (10–100 K) and to have low fractional luminosities ($f < 0.01$). These high fractional luminosities (if we consider $f = \gamma$) is a feature more compatible with young discs compared to those of ordinary debris discs (Wyatt 2008), but the lack of variability seems to be inconsistent with the young-star scenario. On the other hand, extreme debris discs (EDD; Balog et al. 2009), are examples of MIR sources with high fractional luminosities ($f > 0.01$) that have higher temperatures compared to that of standard debris discs (Moór et al. 2021). Nevertheless, these sources have never been observed in connection with M dwarfs. Are our candidates’ strange young stars whose flux does not vary with time? Are these stars M-dwarf debris discs with an extreme fractional luminosity? Or something completely different?

Several searches for infrared sources (e.g. Kennedy et al. 2012; Ribas et al. 2012; Cotten & Song 2016; Theissen & West 2017) have faced challenges in confirming authentic infrared sources. Kennedy et al. (2012) demonstrated a strong correlation between the 100 μm background level from IRIS maps and contamination, setting a 5 MJy/sr threshold to circumvent spurious infrared sources. Fortunately, this was not a concern for our candidates as we utilized

a CNN algorithm, leveraging *W3* images to eliminate sources within nebular regions, typically linked to high levels of FIR radiation near the galactic plane. Detecting infrared sources also raises concerns about potential chance alignments with infrared galaxies, leading to significant *WISE* photometry contamination. Various methods exist to assess the likelihood of encountering such occurrences. Kennedy et al. (2012) compare extragalactic counts to their source counts, while Theissen & West (2017) re-extract sources to compare their *W1/W2/W3* positions. Following the Kennedy et al. (2012) idea, we determine the contamination rate due to background galaxies that could alternatively explain the MIR properties of our candidates. The contamination rate mainly depends on the number of galaxies in the sky per unit of solid angle that can produce a specific signature. In order to determine that value, we compute the number of galaxies with the following properties: *W3/W4* detection with SNRs higher or equal to 3.5, $\text{ext_flg} = 0$, $W1 - W3/W4 > 1.2$ as a colour cut to ensure stars are removed (Jarrett et al. 2011), and $2.84 < W3 - W4 < 3.25$ to ensure galaxies with a colour compatible with that of our DS models for our candidates. The total number of galactic sources per unit of solid angle is $\sim 15\,000$ objects/sr, which yields a contamination rate of 1.1×10^{-5} if we consider a target area of 33 arcsec² (3.25 arcsec of radius). Notice that this contamination rate cannot be applied to the initial sample of $\sim 5 \times 10^6$ since that number does not consider *W3/W4* detection with SNRs higher or equal to 3.5. Instead, we must use it on the sample of stars with *W3/W4* detection and $\text{SNR} \geq 3.5$ in these bands, corresponding to $\sim 200\,000$ sources, which ultimately leads to ~ 2 contaminated sources with the above-listed properties.

Additionally, the offsets between positions within different bands can be used as a tracer of confusion. The offset of a source within all the *WISE* bands should be small, given their similar PSF FWHMs (6'1, 6'4, and 6'5, respectively), and *WISE* astrometric precision of 0'5.² In our analysis of sources, we observed no significant offset between the *W1* and *W2* bands. However, when examining the *W1* and *W3* bands, we noticed a slightly larger offset for some sources. This aligns with the offset distribution reported by Theissen & West (2017), consistent with the offset distribution of quasars. However, candidate G exhibited a higher RA offset than expected. Although this analysis does not indicate a significant shift for six of our candidates, the possibility of perfect alignments cannot be ruled out. Therefore, each source should be approached with caution, and the potential for such alignments should not be dismissed. It is important to note that the shift observed in the seventh object might be attributed to *WISE* confusion, as the contamination rate suggests. *WISE* confusion is quite common (e.g. Denny et al. 2020) and often unavoidable, with studies indicating that it could account for as many as 70 per cent of false positives regarding infrared excesses around main-sequence stars (Silverberg et al. 2018).

Upon examining the colour–magnitude diagram depicted in Fig. 8 alongside our candidates, it is evident that our sample predominantly comprises M dwarfs. However, our candidates deviate from the core of the M dwarf distributions, residing toward the peripheries. The rightward edge aligns more closely with young stars progressing toward the main sequence, while the leftward edge corresponds to the optical dimming anticipated by our models, which can resemble subdwarf stars.

Additional analyses are definitely necessary to unveil the true nature of these sources. Optical spectroscopy has shown to be valuable when refuting false debris disc M dwarf candidates (e.g. Murphy, Mamajek & Bell 2018), and we believe it could help us

²<https://wise2.ipac.caltech.edu/docs/release/allsky/expsup/sec6.4.html>

constrain different features of our sources. $H\alpha$ is typically used to find out whether a star is in a young accreting stage or not. Even though chromospheric activity in M dwarfs can lead to $H\alpha$ emission, the EW of the said line can be used to distinguish accretors from just chromospheric emission (Barrado y Navascués & Martín 2003). In the latter case, the line can be used to determine several M-dwarf characteristics, such as age, stellar rotation, and magnetic activity. Additionally, the intensity of $H\alpha$ in the case of chromospheric activity is a spectral type-dependant feature (e.g. Lépine et al. 2013).

Moreover, gyrochronology can help give us more insight into the ages of our candidates by using stellar rotation as an independent proxy of age since late-type stars' rotation slows down as they age (e.g. Kawaler 1989; Barnes 2003, 2007; Meibom et al. 2015).

5 CONCLUSIONS

After analysing the optical/NIR/MIR photometry of $\sim 5 \times 10^6$ sources, we found seven apparent M dwarfs exhibiting an infrared excess of unclear nature that is compatible with our DS models. We modelled DSs with temperatures ranging from 100 to 700 K and covering factors from 0.1 to 0.9. There are several natural explanations for the infrared excess in literature, but none of them clearly explains such a phenomenon in the candidates, especially given that all are M dwarfs.

We argue that follow-up spectroscopy would help us unveil the nature of these sources. In particular, analysing the spectral region around $H\alpha$ can help us ultimately discard or verify the presence of young discs by analysing the potential $H\alpha$ emission. Spectroscopy in the MIR region would be very valuable when determining whether the emission corresponds to a single blackbody, as we assumed in our models. Additionally, spectroscopy can help us determine the real spectral type of our candidates and ultimately reject the presence of confounders.

We would like to stress that although our candidates display properties consistent with partial DSs, it is definitely premature to presume that the MIR presented in these sources originated from them. The MIR data quality for these objects is typically quite low, and additional data are required to determine their nature.

ACKNOWLEDGEMENTS

The authors first would like to thank the anonymous referees for their extremely helpful comments that greatly improved the quality of this study. MS acknowledges funding from the Royal Swedish Academy of Sciences. MS and EZ acknowledge funding from the Magnus Bergvall Foundation. EZ and CN acknowledge a sabbatical fellowship from AI4Research at Uppsala University. EZ and SM would like to acknowledge financial assistance through the SPARC project no P39 sponsored by the Ministry of Education, Govt. of India. EZ has also benefited from a sabbatical at the Swedish Collegium for Advanced Study. This work has made use of data from the European Space Agency (ESA) mission *Gaia* (<https://www.cosmos.esa.int/gaia>), processed by the *Gaia* Data Processing and Analysis Consortium (DPAC, <https://www.cosmos.esa.int/web/gaia/dpac/consortium>). Funding for the DPAC has been provided by national institutions, in particular the institutions participating in the *Gaia* Multilateral Agreement. This publication makes use of data products from the Two Micron All Sky Survey, which is a joint project of the University of Massachusetts and the Infrared Processing and Analysis Center/California Institute of Technology, funded by the National Aeronautics and Space Administration and the National Science Foundation. This publication makes use of

data products from the Wide-field Infrared Survey Explorer, which is a joint project of the University of California, Los Angeles, and the Jet Propulsion Laboratory/California Institute of Technology, and NEOWISE, which is a project of the Jet Propulsion Laboratory/California Institute of Technology. WISE and NEOWISE are funded by the National Aeronautics and Space Administration. The national facility capability for SkyMapper has been funded through ARC LIEF grant LE130100104 from the Australian Research Council, awarded to the University of Sydney, the Australian National University, Swinburne University of Technology, the University of Queensland, the University of Western Australia, the University of Melbourne, Curtin University of Technology, Monash University and the Australian Astronomical Observatory. SkyMapper is owned and operated by The Australian National University's Research School of Astronomy and Astrophysics. The survey data were processed and provided by the SkyMapper Team at ANU. The SkyMapper node of the All-Sky Virtual Observatory (ASVO) is hosted at the National Computational Infrastructure (NCI). Development and support of the SkyMapper node of the ASVO has been funded in part by Astronomy Australia Limited (AAL) and the Australian Government through the Commonwealth's Education Investment Fund (EIF) and National Collaborative Research Infrastructure Strategy (NCRIS), particularly the National eResearch Collaboration Tools and Resources (NeCTAR) and the Australian National Data Service Projects (ANDS). The Pan-STARRS1 Surveys (PS1) and the PS1 public science archive have been made possible through contributions by the Institute for Astronomy, the University of Hawaii, the Pan-STARRS Project Office, the Max-Planck Society and its participating institutes, the Max Planck Institute for Astronomy, Heidelberg and the Max Planck Institute for Extraterrestrial Physics, Garching, The Johns Hopkins University, Durham University, the University of Edinburgh, the Queen's University Belfast, the Harvard-Smithsonian Center for Astrophysics, the Las Cumbres Observatory Global Telescope Network Incorporated, the National Central University of Taiwan, the Space Telescope Science Institute, the National Aeronautics and Space Administration under grant no. NNX08AR22G issued through the Planetary Science Division of the NASA Science Mission Directorate, the National Science Foundation grant no. AST-1238877, the University of Maryland, Eotvos Lorand University (ELTE), the Los Alamos National Laboratory, and the Gordon and Betty Moore Foundation. The Digitized Sky Survey was produced at the Space Telescope Science Institute under U.S. Government grant NAG W-2166. The images of these surveys are based on photographic data obtained using the Oschin Schmidt Telescope on Palomar Mountain and the UK Schmidt Telescope. The plates were processed into the present compressed digital form with the permission of these institutions. We made use of observations obtained with XMM-Newton, an ESA science mission with instruments and contributions directly funded by ESA Member States and NASA.

DATA AVAILABILITY

Most of the underlying data used in this work is in the public domain (*Gaia*, 2MASS, *WISE*). Models underlying this article are available upon request.

Note added in proof: While this paper was in review, a preprint was published (Contardo & Hogg 2024) which presents a data-driven search for cases of extreme infrared excess in a similarly-sized sample of ~ 5 million stars, also using *Gaia*, 2MASS and *WISE* photometry. Even though their search is sensitive to Dyson spheres, there is no overlap between their final sample of candidates and ours. Their focus is on bright ($G < 16$ mag) FGK stars and objects where

the infrared excess is visible in the WISE W1 and W2 filters, which would correspond to Dyson spheres at higher temperatures than the ones found in our study. The two studies are complementary, as they explore different areas of parameter space.

REFERENCES

- Annis J., 1999, *J. Br. Interplanet. Soc.*, 52, 33
- Avenhaus H., Schmid H. M., Meyer M. R., 2012, *A&A*, 548, A105
- Bailer-Jones C. A. L., Rybizki J., Foesneau M., Demleitner M., Andrae R., 2021, *AJ*, 161, 147
- Balog Z., Kiss L. L., Vinkó J., Rieke G. H., Muzerolle J., Gáspár A., Young E. T., Gorlova N., 2009, *ApJ*, 698, 1989
- Barbary K., 2016, *J. Open Source Softw.*, 1, 58
- Barber M. G., Mann A. W., 2023, *ApJ*, 953, 127
- Barnes S. A., 2003, *ApJ*, 586, 464
- Barnes S. A., 2007, *ApJ*, 669, 1167
- Barrado y Navascués D., Martín E. L., 2003, *AJ*, 126, 2997
- Bertin E., Arnouts S., 1996, *A&AS*, 117, 393
- Carrigan R. A., Jr, 2009, *ApJ*, 698, 2075
- Chambers K. C. et al., 2016, preprint (arXiv:1612.05560)
- Chen H., Garrett M. A., 2021, *MNRAS*, 507, 3761
- Cody A. M. et al., 2014, *AJ*, 147, 82
- Cotten T. H., Song I., 2016, *ApJS*, 225, 15
- Creevey O. L. et al., 2023, *A&A*, 674, A26
- Cronin-Coltsmann P. F. et al., 2022, *MNRAS*, 512, 4752
- Cronin-Coltsmann P. F., Kennedy G. M., Kral Q., Lestrade J.-F., Marino S., Matrà L., Wyatt M. C., 2023, *MNRAS*, 526, 5401
- Cutri R. M. et al., 2014, *VizieR Online Data Catalog*, 328
- Dennihy E., Farihi J., Gentile Fusillo N. P., Debes J. H., 2020, *ApJ*, 891, 97
- Dyson F. J., 1960, *Science*, 131, 1667
- Foesneau M. et al., 2023, *A&A*, 674, A28
- Contardo G., Hogg, D. W., 2024, preprint (arXiv: 2403.18941)
- Gaia Collaboration, 2016, *A&A*, 595, A1
- Gaia Collaboration, 2023, *A&A*, 674, A1
- Garrett M. A., 2015, *A&A*, 581, L5
- Gáspár A., Rieke G. H., 2014, *ApJ*, 784, 33
- Griffith R. L., Wright J. T., Maldonado J., Povich M. S., Sigurdsson S., Mullan B., 2015, *ApJS*, 217, 25
- Heng K., Malik M., 2013, *MNRAS*, 432, 2562
- Herbst W., Eislöffel J., Mundt R., Scholz A., 2007, in Reipurth B., Jewitt D., Keil K., eds, *Protostars and Planets V*. University of Arizona Press, Tucson, p. 297
- Hinton G. E., Srivastava N., Krizhevsky A., Sutskever I., Salakhutdinov R. R., 2012, preprint (arXiv:1207.0580)
- Hsiao T. Y.-Y. et al., 2021, *MNRAS*, 506, 1723
- Huston M. J., Wright J. T., 2022, *ApJ*, 924, 78
- Ioffe S., Szegedy C., 2015, in *Proceedings of the 32nd International Conference on International Conference on Machine Learning – Vol. 37, ICML’15*. JMLR.org, p. 448
- Jarrett T. H. et al., 2011, *ApJ*, 735, 112
- Joy A. H., 1945, *ApJ*, 102, 168
- Jugaku J., Nishimura S., 1991, *Lecture Notes in Physics Vol. 390*, Springer, Berlin, p. 295
- Jugaku J., Nishimura S., 2004, in Norris R., Stootman F., eds, *Proc. IAU Symp. 213, Bioastronomy 2002: Life Among the Stars*. Kluwer, Dordrecht, p. 437
- Kawaler S. D., 1989, *ApJ*, 343, L65
- Kennedy G. M. et al., 2018, *MNRAS*, 476, 4584
- Kennedy G. M., Wyatt M. C., 2013, *MNRAS*, 433, 2334
- Kennedy G. M., Wyatt M. C., Sibthorpe B., Phillips N. M., Matthews B. C., Greaves J. S., 2012, *MNRAS*, 426, 2115
- Kingma D. P., Ba J., 2014, preprint (arXiv:1412.6980)
- Krivov A. V. et al., 2013, *ApJ*, 772, 32
- Lacki B. C., 2016, preprint (arXiv:1604.07844)
- Lang D., 2014, *AJ*, 147, 108
- Lépine S., Hilton E. J., Mann A. W., Wilde M., Rojas-Ayala B., Cruz K. L., Gaidos E., 2013, *AJ*, 145, 102
- Luppe P., Krivov A. V., Booth M., Lestrade J.-F., 2020, *MNRAS*, 499, 3932
- Meibom S., Barnes S. A., Platais I., Gilliland R. L., Latham D. W., Mathieu R. D., 2015, *Nature*, 517, 589
- Miville-Deschênes M.-A., Lagache G., 2005, *ApJS*, 157, 302
- Moór A. et al., 2021, *ApJ*, 910, 27
- Murphy S. J., Mamajek E. E., Bell C. P. M., 2018, *MNRAS*, 476, 3290
- Nair V., Hinton G. E., 2010, in *Proceedings of the 27th International Conference on International Conference on Machine Learning, ICML’10*. Omnipress, Madison, WI, USA, p. 807
- Neugebauer G. et al., 1984, *ApJ*, 278, L1
- Olson S. J., 2017, *Int. J. Astrobiol.*, 16, 176
- Onken C. A. et al., 2019, *Publ. Astron. Soc. Aust.*, 36, e033
- Osmanov Z., 2016, *Int. J. Astrobiol.*, 15, 127
- Osmanov Z., 2018, *Int. J. Astrobiol.*, 17, 112
- Paszke A. et al., 2019, in *Advances in Neural Information Processing Systems 32*, Curran Associates, Inc., Vancouver, Canada, 7994
- Patel R. I., Metchev S. A., Heinze A., 2014, *ApJS*, 212, 10
- Plavchan P., Jura M., Lipsy S. J., 2005, *ApJ*, 631, 1161
- Riaz B., Mullan D. J., Gizis J. E., 2006, *ApJ*, 650, 1133
- Ribas Á., Merín B., Ardila D. R., Bouy H., 2012, *A&A*, 541, A38
- Sciortino S., 2022, *Handbook of X-ray and Gamma-ray Astrophysics*, Springer, Singapore, 74, Star-Forming Regions
- Semiz İ., Oğur S., 2015, preprint (arXiv:1503.04376)
- Sgro L. A., Song I., 2021, *MNRAS*, 508, 3084
- Silverberg S. M. et al., 2018, *ApJ*, 868, 43
- Skrutskie M. F. et al., 2006, *AJ*, 131, 1163
- Slysh V. I., 1985, in Papagiannis M. D., ed., *Proc. IAU Symp. 112, The Search for Extraterrestrial Life: Recent Developments*. Kluwer, Dordrecht, p. 315
- Stassun K. G., Torres G., 2021, *ApJ*, 907, L33
- Suazo M., Zackrisson E., Wright J. T., Korn A. J., Huston M., 2022, *MNRAS*, 512, 2988
- Theissen C. A., West A. A., 2017, *AJ*, 153, 165
- Thompson M. A., Weinberger A. J., Keller L. D., Arnold J. A., Stark C. C., 2019, *ApJ*, 875, 45
- Timofeev M. Y., Kardashev N. S., Promyslov V. G., 2000, *Acta Astronaut.*, 46, 655
- Vioque M., Oudmaijer R. D., Schreiner M., Mendigutía I., Baines D., Mowlavi N., Pérez-Martínez R., 2020, *A&A*, 638, A21
- Weinberger A. J., 2008, *ApJ*, 679, L41
- Wright E. L. et al., 2010, *AJ*, 140, 1868
- Wright J. T., 2020, *Serb. Astron. J.*, 200, 1
- Wright J. T., Cartier K. M. S., Zhao M., Jontof-Hutter D., Ford E. B., 2016, *ApJ*, 816, 17
- Wright J. T., Griffith R. L., Sigurdsson S., Povich M. S., Mullan B., 2014b, *ApJ*, 792, 27
- Wright J. T., Mullan B., Sigurdsson S., Povich M. S., 2014a, *ApJ*, 792, 26
- Wyatt M. C., 2008, *ARA&A*, 46, 339
- Zackrisson E., Calissendorff P., Asadi S., Nyholm A., 2015, *ApJ*, 810, 23
- Zackrisson E., Korn A. J., Wehrhahn A., Reiter J., 2018, *ApJ*, 862, 21
- Zuckerman B., 2022, *MNRAS*, 514, 227

APPENDIX A: SELECTION OF STARS

In order to construct our set of DS models, we start from a set of observed stars with available Gaia DR3-2MASS-AllWISE photometry and bolometric luminosities. We select a sample of 265 main-sequence stars within 100 pc of the Sun. To ensure the selection of main-sequence stars, we apply the same criteria as Suazo et al. (2022), which exclude red giants, white dwarfs, and sources with high astrometric excess noise. The filtering process is defined by equation (A1) for removing red giants and equation (A2) for eliminating white dwarfs and sources with high astrometric excess noise. In these equations, M_G represents the absolute magnitude of the star in

the G band, and $G_{\text{BP}} - G_{\text{RP}}$ denotes its colour, both measured in the Vega system.

$$M_G < 4 \text{ and } M_G < 7 \cdot (G_{\text{BP}} - G_{\text{RP}}) - 3, \quad (\text{A1})$$

$$M_G > 3 \cdot (G_{\text{BP}} - G_{\text{RP}}) + 5. \quad (\text{A2})$$

In addition to the cuts ensuring only main-sequence stars, we consider only stars with flux measurements available in all relevant bands and a RUWE below 1.4, ensuring that the astrometric solution is of high quality. Additionally, we include stars with FLAME luminosity estimations (Creevey et al. 2023; Fouesneau et al. 2023), which are necessary for our models. We exclude stars with contamination in their *WISE* photometry and stars already exhibiting an MIR excess. To ensure a diverse sample, we restrict our selection to stars with absolute magnitudes (M_G) ranging from 0 to 13.6, corresponding to zero-age main sequence masses between approximately 0.15 and 3.5 solar masses (M_\odot). Outside of this range, no stars meet the aforementioned criteria. We also selected the sample to homogeneously distribute the number of stars in the magnitudes range.

Additionally, to ensure our photometric measurements' accuracy, we considered the saturation limits for the *WISE* bands when selecting the main-sequence stars. Sources brighter than 8.1, 6.7, 3.8, and -0.4 mag (Vega) in $W1$, $W2$, $W3$, and $W4$, respectively, are known to be saturated, resulting in overestimated fluxes. To mitigate this effect, we applied the $W2$ correction proposed by Cotten & Song (2016) specifically for the $W2$ band. However, our analysis found no significant difference when considering corrected and uncorrected $W2$ fluxes. This is primarily because our sources are located in the unsaturated regime, where the flux measurements are reliable without the need for correction.

We applied DS models with temperatures ranging from 100 to 700 K and covering factors between 0.1 and 0.9 for each selected star. Since we have 265 stars, 17 covering factors, and 49 temperatures, we end up with 220 745 models, 833 for each star (17 covering factors and 49 temperatures). Please see Fig. 2 for an example of how the model parameters alter the SED of a Sun-like star.

This paper has been typeset from a $\text{\TeX}/\text{\LaTeX}$ file prepared by the author.